MCUR1-CCDC90B complex is a conserved regulator of metabolic homeostasis

Ferreira J Verissimo[1,#], Wettmarshausen J[1,#], Goh V[1], Feng MS[1], Lagerborg K[2], Delgado de la Herran H[1], Walia S[1], Cheng Y[1], Leimpek A[1], Gorza M[1], Braun S[3], Nilsson R[4], Jain M[2], Mann M[5,6], Mokranjac D[7,8], Murgia M[5,9], Haack TB[10,11], Deschauer M[12], Prokisch H[13,14], Filipp FV[15,16,17,*] and Perocchi F[1,18,19,20,*]

[1]Institute for Diabetes and Obesity, Helmholtz Diabetes Center, Helmholtz Munich, Munich, Germany
[2]Departments of Medicine and Pharmacology, UC San Diego School of Medicine, La Jolla, CA, USA
[3]Institute for Genetics, Justus-Liebig-University Giessen, Giessen, Germany
[4]Department of Medicine, Karolinska Institute, Karolinska University Hospital, Stockholm, Sweden
[5]Department of Proteomics and Signal Transduction, Max Planck Institute of Biochemistry, Martinsried, Germany
[6]Faculty of Health Sciences, Novo Nordisk Foundation Center for Protein Research, University of Copenhagen, Copenhagen, Denmark
[7]LMU Munich, Biozentrum-Cell Biology, Planegg-Martinsried, Germany
[8]BioMedical Center (BMC), Division of Physiological Chemistry, Faculty of Medicine, LMU Munich, Planegg-Martinsried, Germany
[9]Department of Biomedical Sciences, University of Padova, Padua, Italy
[10]Institute of Medical Genetics and Applied Genomics, University of Tübingen, Tübingen, Germany
[11]Centre for Rare Diseases, University of Tuebingen, Tübingen, Germany
[12]Department of Neurology, Klinikum rechts der Isar, School of Medicine and Health, Technical University of Munich, Munich, Germany
[13]Institute of Neurogenomics, Computational Health Center, Helmholtz Munich, Munich, Germany
[14]School of Medicine, Institute of Human Genetics, Technical University of Munich, Munich, Germany
[15]School of Life Sciences Weihenstephan, Technical University of Munich, Freising, Germany
[16]Institute for Advanced Study, Technical University of Munich, Munich, Germany
[17]Metaflux, San Diego, CA, USA
[18]German Center for Diabetes Research, Munich, Germany
[19]Institute of Neuronal Cell Biology, Technical University of Munich, Munich, Germany.
[20]Munich Cluster for Systems Neurology, Munich, Germany

[#]These authors contributed equally
*Co-corresponding authors

ABSTRACT

The mitochondrial calcium uniporter regulator 1 (MCUR1) is an evolutionarily conserved protein of the inner mitochondrial membrane whose physiological role remains elusive. Although initially proposed as a subunit of the mitochondrial calcium uniporter complex (MCUC), emerging evidence suggests that MCUR1 has a broader functional outreach. Here, we identify a biallelic loss-of-function *MCUR1* variant in a patient displaying neurological defects, which leads to loss of MCUR1 protein and exerts a dominant negative effect on its paralog CCDC90B. MCUR1 and CCDC90B form a stable hetero-oligomeric complex, whose stability depends on MCUR1. Despite preserved mitochondrial respiration, calcium uptake, and membrane potential, MCUR1-deficient human cells and yeast models exhibit impaired lipid and amino acid metabolism, leading to proliferative delay. Patient serum metabolomics

confirm elevated amino acid levels, and yeast deletion mutants show nitrogen source-dependent growth defects that are rescued by expression of human MCUR1. These findings redefine the MCUR1-CCDC90B as a mitochondrial scaffold critical for membrane protein complexes and metabolic homeostasis and suggest a potential link between MCUR1 deficiency and neurometabolic disease.

INTRODUCTION

MCUR1 (previously annotated as CCDC90A) and its paralog CCDC90B belong to a functionally heterogeneous family of coiled-coil domain-containing (CCDC) proteins implicated in scaffolding, membrane fusion, and signal transduction (Adlakha et al., 2019). Despite strong evolutionary conservation, the function of MCUR1 and CCDC90B remains unclear (Garbincius & Elrod, 2021). Loss of MCUR1 in mammalian cell lines and heart mitochondria impairs mitochondrial Ca^{2+} (mt-Ca^{2+}) uptake by destabilizing MCUC assembly (Mallilankaraman et al., 2012; Tomar et al., 2016; Vais et al., 2015). By contrast, overexpression of human MCUR1 in *Drosophila* cells, which lack MCUR1 homologs, reduces mt-Ca^{2+} buffering capacity and sensitize mitochondria to Ca^{2+}-induced permeability transition, likely through a direct interaction with components of the mitochondrial permeability transition pore (MPTP) (Chaudhuri et al., 2016). Studies in human fibroblasts and in the budding yeast *Saccharomyces cerevisiae* have challenged this Ca^{2+}-centric model, proposing instead that MCUR1 may either regulate the assembly of respiratory chain complex (RCC) IV (cytochrome c oxidase) (Paupe et al., 2015) or modulate proline utilization (Zulkifli et al., 2020). The reported effects of MCUR1 loss-of-function on mt-Ca^{2+} uptake may therefore reflect perturbations in cellular bioenergetics and mitochondrial membrane potential. Collectively, these observations raise fundamental questions about the primary function of MCUR1 and its potential relevance to human physiology.

Here, we report the identification of a patient with predicted loss-of-function variant in *MCUR1*. This variant abolishes the expression of both MCUR1 and CCDC90B. Through integrative systems analyses in patient-derived fibroblasts, HeLa cells, and two evolutionarily distant yeast models (*Saccharomyces cerevisiae* and *Schizosaccharomyces pombe)*, we demonstrate that MCUR1 is dispensable for mt-Ca^{2+} uptake, Ca^{2+} buffering, and respiratory activity. Instead, it plays a conserved role in anabolic metabolism and stress response. These findings redefine MCUR1 as a foundational mitochondrial membrane and metabolic regulator rather than reducing its role to a core component of the MCUC, with potential implications for understanding and treating human disease.

MCUR1 loss-of-function variant in a rare disease patient with neurological phenotype

We identified a 31-year-old male with a biallelic variant in *MCUR1*, presenting with a neurological disorder of early-adult-onset (25 years) and slow clinical progression (**Fig. 1A**). The patient exhibited impaired balance and vision, with bilateral internuclear ophthalmoplegia, vertical nystagmus, brisk deep tendon reflexes, bilateral Babinski sign, cerebellar ataxia, and pathological laughter. However, we did not observe any brain abnormalities by needle electromyography, magnetic resonance spectroscopy, cell count analysis, and measurements of protein and lactate levels in the cerebrospinal fluid (**Fig. 1A**). Instead, magnetic resonance imaging (MRI) clearly indicated symmetric bilateral hyperintensities of the pyramidal tract in both the internal capsule and in the brainstem, as well as lesions affecting the medial longitudinal fasciculus (**Fig. 1B**). Altogether, metabolic, sensory, and histological examinations ruled out the diagnosis of a classical disorder of the mitochondrial oxidative phosphorylation system (OXPHOS), given that routine blood tests

and photometric analyses of muscle biopsies showed normal levels of creatine kinase and lactate, cytochrome c oxidase (COX)/succinate dehydrogenase (SDH) staining, respiratory chain complex activity, and mitochondrial DNA sequence. Exome sequencing performed on total genomic DNA extracted from peripheral blood leucocytes identified a homozygous c.802C>T variant in *MCUR1* (ENST00000379170.9), which was confirmed by Sanger sequencing (**Fig. 1C**). As shown by the pedigree of the patient's consanguineous family (**Fig. 1D**), five of the seven healthy siblings were heterozygous carriers of the same variant, whereas a 19-year-old sister (subject II-8) was a homozygous carrier but without apparent clinical signs at the time of the investigation. This c.802C>T substitution is listed 38 times in a heterozygous state in the Genome Aggregation Database (gnomAD) project and an in-house database, containing 1.607.006 and 14.000 alleles, respectively. While the minor allele frequency of the c.802C>T variant is concordant with an autosomal recessive trait, we cannot exclude a higher prevalence in the ancestral population, which is presumably underrepresented in publicly accessible databases.

MCUR1 contains at the N-terminus a predicted mitochondrial targeting sequence and a putative transmembrane region. The C-terminal faces the matrix side and is arranged in a coil-coiled structure followed by a second transmembrane domain that anchors the protein to the inner mitochondrial membrane (IMM) (**Fig. 1E**). The biallelic c.802C>T *MCUR1* variant is predicted to result in loss-of-function by introducing an Arg268Ter (R268X) substitution in the coil-coiled domain of MCUR1. Immunoblotting analysis showed that the R268X substitution dramatically affected the level of both MCUR1 and CCDC90B proteins, compared to three unrelated control lines from unaffected individuals (**Fig. 1F, G**). By introducing an intron-less $MCUR1^{R268X}$ isoform in the patient skin fibroblasts, we could restore the expression of a truncated MCUR1 version (**Fig. 1F**), indicating nonsense mediated mRNA decay of the *MCUR1* c.802C>T variant.

MCUR1 deficiency does not impair mt-Ca^{2+} uptake and mitochondrial respiration

To test the proposed role of MCUR1 in mt-Ca^{2+} regulation, we quantified mt-Ca^{2+} transients in intact and permeabilized patient fibroblasts using a mitochondrial matrix-targeted aequorin (mt-AEQ) as a luminescent Ca^{2+} sensor. Upon stimulation with histamine, which triggers Ca^{2+} release from the endoplasmic reticulum (ER), both patient and control fibroblasts displayed similar mt-Ca^{2+} uptake kinetics (**Fig. 2A**). To exclude the influence of genetic background, we generated isogenic HeLa cell lines expressing small hairpin RNAs (shRNAs) against MCUR1 and confirmed no effect in absence of MCUR1 (**Fig. S1A,B**). To evaluate whether the lack of a mt-Ca^{2+} phenotype reflected compensatory changes in upstream Ca^{2+} signalling, we measured Ca^{2+} transients after selective plasma membrane permeabilization with digitonin and depletion of intracellular Ca^{2+} stores by the SERCA inhibitor thapsigargin in presence of EGTA. mt-Ca^{2+} uptake kinetics triggered by an exogenous Ca^{2+} bolus were comparable between control and patient fibroblasts, regardless of whether mitochondria were energized with RCCI (**Fig. 2B**) or RCCIV-specific substrates (**Fig. S1C**). Similarly, fluorescence-based measurements of Ca^{2+} clearance using the non-permeable dye Ca-Green-5N revealed no difference in the rate of signal decay between control and patient cells (**Fig. 2C**). Given previous evidence linking MCUR1 to the regulation of MPTP (Chaudhuri et al., 2016), we examined mt-Ca^{2+} buffering in patient fibroblasts. The timing and extramitochondrial Ca^{2+} concentration required to trigger mitochondrial swelling did not differ between patients and control cells (**Fig. S1D**). We next assessed whether compensatory adaptations in MCUC might account for the lack of phenotype. Expression level of known MCUC subunits were unchanged in both patient fibroblasts (**Fig. S2A)** and shMCUR1 HeLa cells (**Fig. S2B)**.

Similarly, MCUR1 deficiency did not affect MCUC complex assembly (**Fig. S2C, D**). Together, these physiological and biochemical analyses suggest that MCUR1 is dispensable for mt-Ca^{2+} uptake in primary human fibroblasts and stable shMCUR1 HeLa cells.

Earlier studies reported conflicting roles for MCUR1 in the biogenesis of RCC IV (Paupe et al., 2015; Vais et al., 2015). Although patient symptoms and muscle biopsy findings did not indicate OXPHOS deficiency, we examined mitochondrial bioenergetics in patient fibroblasts. Measurements of oxygen consumption rates (OCR) revealed no differences in basal, non-ADP-stimulated, or carbonyl cyanide m-chlorophenylhydrazone (CCCP)-uncoupled respiration between patient and control cells (**Fig. S3A**), or upon fuelling respiration with substrates specific for RRCI (**Fig. S3B**), RCCII (**Fig. S3C**), or RCCIV (**Fig. 2D**). Moreover, shMCUR1 HeLa cells showed only minor reductions in basal and CCCP-stimulated respiration (**Fig. S3D**). Consistently, expression of individual RCC subunits was unaffected in both patient fibroblasts (**Fig. 2E**) and shMCUR1 HeLa cells (**Fig. S4A**), likewise their assembly (**Fig. S4B, C**).

Finally, we employed the budding yeast *Saccharomyces cerevisiae* as a model system (**Fig. S5**). Deletion of the MCUR1 homolog *FMP32/PUT6* in two genetic backgrounds (BY4742 and YPH499) did not impair growth on both solid (**Fig. S5A**) and liquid (**Fig. S5B**) media containing fermentable (glucose, YPD) or non-fermentable (glycerol, YPG; lactate YPL) carbon sources at three tested temperatures (24°C, 30°C, and 37°C). These results are consistent with previous findings (VanderSluis et al., 2014) and confirm that mitochondrial bioenergetics and respiratory chain activity are fully functional in *fmp32*Δ strains. Together, our data from human primary skin fibroblasts, isogenic HeLa cells, and yeast knockout strains indicate that MCUR1 is dispensable for mt-Ca^{2+} homeostasis and respiratory metabolism.

MCUR1 forms a hetero-oligomeric complex with CCDC90B

To elucidate MCUR1's molecular function, we interrogated its protein interaction network. We engineered a stable HEK-293 cell line expressing C-terminally tagged MCUR1 at near-endogenous levels (**Fig. S6A**). Subcellular fractionation (**Fig. S6B)**, carbonate extraction (**Fig. S6C**), and protease protection assays (**Fig. S6D**) confirmed correct mitochondrial targeting and membrane topology of the tagged protein, which was subsequently used as bait for protein complex analysis. Next, we performed tandem affinity purifications (TAP) using C-terminal Strep II and His_6 tags, followed by LC-MS/MS analysis. Five biological replicates, including parental HEK-293 cells as negative controls, allowed discrimination between specific and nonspecific interactions. As shown in **Fig. S6E**, CCDC90B was the most significantly enriched and reproducible MCUR1 interactor. Consistently, BN-PAGE of crude mitochondrial fractions from control fibroblasts revealed a high-molecular-weight complex containing both MCUR1 and CCDC90B, which was absent in patient fibroblasts (**Fig. S6F**). Moreover, CCDC90B protein levels were drastically reduced in sh-MCUR1 HeLa cells (**Fig. S6G**), demonstrating that formation and stability of the complex depend on MCUR1.

Loss of MCUR1 and CCDC90B homologs in the fission yeast *Schizosaccharomyces Pombe* disrupts amino acid and nitrogen metabolism

To explore the functional relationship between MCUR1 and CCDC90B, we analysed their conservation across 247 fully sequenced eukaryotes (**Fig. S7**). MCUR1 homologs are present in nearly all vertebrates, fungi, and plants but arthropods, apicomplexa (e.g., *Plasmodium falciparum*), and mitochondrial-lacking protists (e.g., *Entamoeba histolytica*,

Giardia lambia, *E. cuniculi*). In contrast, CCDC90B displays a more restricted distribution, co-occurring with MCUR1 mainly in vertebrates, plants, and few filamentous fungi such as the fission yeast *Schyzosaccharomyces pombe* (S. pombe).

Given the conservation of signalling and metabolic pathways in *S. pombe*, we used it as a model to investigate MCUR1 and CCDC90B functions. We identified three related *S. pombe* sequences: *Sp-MCUR1* (*SPAC2C4.09*) and *Sp-CCDC90B* (*SPAC3H1.08c*), paralogous to human *MCUR1* and *CCDC90B*, and *SPBC27B12.07*, which belongs to a distinct fungal clade (**Fig. 3A**). Notably, Sp-CCDC90B had been previously linked to the function of target of rapamycin complex 1 (TORC1) (Rallis et al., 2013), while the *S. cerevisiae* homolog FMP32 was shown to affect growth on arginine and proline as sole nitrogen sources (VanderSluis et al., 2014). To test whether *Sp-MCUR1* and *Sp-CCDC90B* contribute to nitrogen metabolism, we generated single and double deletion mutants in the prototrophic strain 972h. Prototrophic strains have the ability to synthesize organic building blocks from inorganic sources when cultured in defined minimal essential media conditions. When cultured in minimal medium with glucose as carbon source and ammonium sulphate as the sole nitrogen source, both mutants exhibited severe growth defects compared to wild type (**Fig. 3B**), partially rescued by proline supplementation. Instead, wild type and mutant strains grew similarly in presence of downstream proline-derived metabolites such as arginine (**Fig. S8A**) or glutamate (**Fig. S8B**). Accordingly, the growth phenotype of *Sp-MCUR1* deletion mutant was fully restored when ammonium sulphate and glutamate were supplemented together (**Fig. S8C**).

Untargeted metabolomic profiling using stable isotope assisted enrichment with ^{14}N and ^{15}N ammonium sulfate as sole carbon source uncovered significant alterations in lipid and amino acid metabolism, including pathways for glycerophospholipids, fatty acid conjugates, arginine, proline, alanine, aspartate, glutamate, nicotine amide, purine, polyamine, and glutathione (**Figure 3C-E**). Proline-related metabolites and dipeptides were particularly enriched, indicating dysregulated proline metabolism. Expression of human MCUR1, but not human CCDC90B, restored normal growth in both single and double mutants (**Fig. 3F**), demonstrating that MCUR1 plays a conserved role in amino-acid metabolism and exerts a dominant functional effect over CCDC90B.

MCUR1 deficiency in humans results in impaired amino acid metabolism

To evaluate the systemic effects of MCUR1 deficiency, we performed untargeted metabolomics profiling of patient serum and compared metabolite levels to reference datasets representing normal physiological states, including fasting, dietary intake, physical activity, and standardized metabolic challenge tests (**Fig. 4A**). Proline, carnitine, valine, and isoleucine were significantly elevated ($p < 0.05$), with enrichments of arginine and proline metabolism pathways (**Fig. 4B**). We also observed dysregulation of the urea cycle, ammonia recycling, glutamate and aspartate metabolism, spermidine/spermine biosynthesis, glutathione metabolism, and the tricarboxylic acid (TCA) cycle ($p< 0.05$). Complementary whole-cell proteomics of patient fibroblasts and MCUR1 knockdown HeLa cells (**Fig. 4C, D**) showed upregulation of autophagy, vacuolar and epithelial mesenchymal transition (EMT) processes, as well as proline metabolism, alongside downregulation of cell cycle regulators, E2F target proteins, and mitochondrial metabolism. Together, these multi-omics signatures indicated a disturbance in non-essential amino acid metabolism and suggested a biosynthetic bottleneck in MCUR1-deficient cells, potentially mitigated by amino acid salvage pathways. To test this, we performed *in vitro* wound-healing assays using control and MCUR1-deficient fibroblasts cultured in minimal media without non-essential amino acids

(**Fig. 4E**). Patient fibroblasts displayed a pronounced delay in growth and migration, which was fully rescued by MCUR1 re-expression (**Fig. 4F, G**). Collectively, these findings demonstrate that *MCUR1* deficiency perturbs non-essential amino acid metabolism and limits anabolic support, particularly proline biosynthesis.

DISCUSSION

The molecular function of MCUR1 has remained controversial, despite a decade of intensive study. Through an integrated approach combining human genetics, patient-derived cells, and evolutionary distant yeast models, we provide compelling evidence that human MCUR1 is dispensable for mt-Ca^{2+} uptake and respiratory chain assembly but acts as a conserved regulator of mitochondrial lipid and amino acid metabolism. The proposal that MCUR1 is a core subunit of the MCUC arose largely from co-immunoprecipitation studies using overexpressed proteins. However, several unbiased proteomics screens of MCUC-associated proteins failed to detect stable interactions between MCUR1 and MCU under near-endogenous expression conditions (Delgado de la Herran et al., 2024) or when only one protein was used as a bait (Delgado de la Herran et al., 2024; Sancak et al., 2013). Consistent with this, we found that MCUR1 forms a stable hetero-oligomeric complex with CCDC90B, whose stability depends on MCUR1. Moreover, phylogenomic analyses have reported that the MCUC is lost in fungi (Pittis et al., 2020), implying that MCUR1 homologues exist in absence of MCUC and perform mt-Ca^{2+}-independent functions. A second line of evidence proposed that MCUR1 contributes to respiratory chain biogenesis, specifically cytochrome c oxidase assembly (Paupe et al., 2015). Paupe at al. reported respiratory defects following MCUR1 depletion in mammalian cells, and loss of Fmp32, the homolog in S. cerevisiae, was associated with impaired growth on non-fermentable carbon sources. Our data contradict this model. Using two independent *fmp32*Δ alleles generated with distinct selection markers, tested in two yeast backgrounds and three temperatures, we observed no respiratory growth defect, consistent with previous findings showing intact mitochondrial bioenergetics in the absence of Fmp32 (VanderSluis et al., 2014). Hence, MCUR1 is unlikely to act as a general assembly factor for cytochrome c oxidase.

Our multi-omics profiling reveals a conserved role for MCUR1 in mitochondrial metabolism, particularly phospholipid, glutamate, arginine, and proline salvage. In fission yeast, MCUR1 deletion causes severe growth impairment on ammonium sulphate as the sole nitrogen source, a condition in which de novo biosynthetic pathways must provide nitrogenous amino acids. Together with the dependency of CCDC90B stability on MCUR1, these findings highlight an evolutionary conservation of its function. Metabolomics analyses of patient's serum showed elevations in proline and branched-chain amino acids, and disruption of urea cycle, spermidine, and glutathione pathways and whole-cell proteomics revealed activation of autophagy-related pathways, further supporting a systemic role in amino acid homeostasis. Under nutrient limiting conditions, the delayed wound healing and proliferative arrest in MCUR1-deficient fibroblasts was rescued by MCUR1 re-expression, a result that underscores the functional consequence of defective anabolic and anaplerotic support. We propose a working model in which MCUR1 (together with CCDC90B) serves as a mitochondrial scaffold or assembly platform that couples mitochondrial biogenesis to biosynthetic capacity. In this view, MCUR1 loss compromises the mitochondrial membrane, thereby affecting lipid composition and ability to assimilate or regulate metabolism. In response, compensatory mechanisms such as autophagy, salvage pathways, and stress responses are activated to sustain cell growth and proliferation. In line with this interpretation, MCUR1 is highly expressed in energy demanding organs such as brain, liver, and heart

(Jiang et al., 2020), which rely heavily on lipid and amino acid metabolism to sustain biosynthetic and redox balance. The brain, in particular, depends on lipid, glutamate, glutamine, and branch-chain amino acids for neurotransmission and neurotransmitter precursors synthesis.

The study clearly establishes oligomerization and substrate specificity of the MCUR1–CCDC90B complex. Within the mitochondrial life cycle, MCUR1 can interact with or stabilize one or more mitochondrial components, transporter subunits, biosynthetic factors, metabolic enzymes, or transient multimeric complexes. Limitations of the study include that we cannot exclude tissue-specific roles or compensation in different comorbidities or due to metabolic plasticity. Finally, developmental, dietary, or epigenetic differences may modulate severity and phenotypic variability, such as seen in the patient's younger sister who is homozygous but remains largely asymptomatic to date. Future work should delineate how MCUR1–CCDC90B complexes coordinate lipid and amino acid metabolism with stress responses and autophagy, and whether these biochemical perturbations underlie the neurological manifestations in affected patients.

MAIN FIGURE LEGENDS

Fig. 1. Identification of a *MCUR1* loss-of-function mutation in a consanguineous family.

(A) Summary of clinical findings of the patient.

(B) Bilateral hyperintensities (red arrow heads) of the internal capsule (*left*: pyramidal tract) and the medial longitudinal fasciculus (*right*: brain stem) identified by T2-weighted MRI scans of the patient's brain.

(C) Biallelic c.802C>T *MCUR1* variant identified from whole-exome sequencing of patient's genomic DNA with illustrative chromatogram.

(D) Pedigree of the patient's (II-2) consanguineous family. Males and females are shown by squares and circles, respectively, and their age is indicated below. Filled and half-filled symbols refer to family members with the homozygous or heterozygous $MCUR1^{c.802C>T}$ variant. The affected sibling is marked in red. Parents have not been sequenced.

(E) Domain structure of MCUR1 highlighting a mitochondrial targeting sequence (MTS), two transmembrane domains (TM), and a coiled-coil domain (CCD). The arrow indicates the mutation introduced by the variant.

(F) Immunoblot analysis of MCUR1 in lysates of primary skin fibroblasts from either three unrelated controls or patient, upon exogenous expression of wild-type MCUR1 or $MCUR1^{R268X}$ variant. ß-actin is used as loading control. *, truncated variant of MCUR1.

(G) Immunoblot analysis of CCDC90B in lysates of primary skin fibroblasts from one unrelated control or patient (n=4 technical replicates). ß-actin is used as loading control.

Fig. 2. Mitochondrial Ca^{2+} uptake and bioenergetics are preserved in patient fibroblasts.

(A) Average traces and quantification of mt-Ca^{2+} transients in controls and patient skin fibroblasts stably expressing mt-AEQ upon histamine (His) stimulation.

(B) Average traces and quantification of mt-Ca^{2+} uptake in digitonin-permeabilized controls and patient skin fibroblasts in presence of glutamate (10 mM) and malate (2 mM) as respiratory substrates.

(C) Average traces of mt-Ca^{2+} buffering capacity in digitonin-permeabilized controls and patient skin fibroblasts in presence of glutamate (10 mM) and malate (2 mM) as respiratory

substrates. Ru360 (10 µM) was used as positive control for MCU inhibition (***p<0.001; one-way ANOVA with Tukey's multiple comparisons test).

(D) Measurements of RCCIV-dependent OCR in digitonin-permeabilized patient and control fibroblasts. (*Left*) Average OCR kinetics and (*right*) quantification of basal (State II), ADP-stimulated (State III), non-ADP-stimulated (State IV_o) and CCCP-stimulated (State III_u) respiration in response to ADP (4 mM), oligomycin A (O, 1.5 µM), and CCCP (C, 15 µM) and in presence of TMPD (0.5 mM)/ ascorbate (2 mM) as respiratory substrates and antimycin A (2 µM) as RCCIII inhibitor. Azide (Az, 20 uM) was used to block RCCIV-driven respiration. Data are normalized by total DNA content (*N*= 3 biologically independent experiments with more than 4 technical replicates for each condition).

(E) Immunoblot analysis of individual RCC subunits in whole-cell lysates from controls and patient fibroblasts. ß-actin is used as loading control (*N*= 3 biologically independent experiments).

All data represent mean ± SEM and refer to *N*> 3 biologically independent experiments.

Fig. 3. Impairment of lipid and amino acids metabolism by MCUR1 loss-of-function is conserved from yeast to human.

(A) *S. pombe* orthologs of human MCUR1 (SPAC2C4.09) and CCDC90B (SPAC3H1.08c), here referred to as Sp-MCUR1 and Sp-CCDC90B respectively, were confirmed by profile hidden Markov Models HMMsearch using the DUF1640 protein domain, which is conserved to all retrieved sequences.

(B) Growth of prototrophic *S. pombe* wild-type (WT) and knockout strains lacking either MCUR1 (Sp-MCUR1 KO), CCDC90B (Sp-CCDC90B KO), or both (Sp-Double KO) in minimal media with either ammonium sulphate or proline as sole nitrogen source (*N*= 4 biologically independent experiments; ***p < 0.001, one-way ANOVA with Dunnett's multiple comparisons test).

(C) Untargeted stable isotope metabolomics analysis highlights enrichment of ^{15}N stable isotope label in proline metabolites. Metabolomics profiling of WT versus Sp-MCUR1 and Sp-CCDC90B double knockout strains grown in minimal media with ammonium sulfate by untargeted and ^{15}N stable isotope labelling LC-MS.

(D) Pathway enrichment analysis of untargeted and ^{15}N stable isotope labelled metabolite analysis.

(E) Metabolic network and pathway analysis of stable isotope enriched metabolomics data.

(F) *Homo sapiens* MCUR1 can functionally complement *S. pombe* single and double Sp-MCUR1 and Sp-CCDC90B knockout mutants and rescue their growth defect in minimal media supplemented with ammonium sulphate as sole nitrogen source (*N*= 4 biologically independent experiments; ***p < 0.001, one-way ANOVA with Dunnett's multiple comparisons test).

All data represent mean ± SEM.

Figure 4. Multi-omics analysis identifies a dysregulation of amino acid metabolism in humans.

(A) Metabolic profiling of serum samples from the patient and a set of healthy controls from HuMet repository.

(B) Pathway enrichment analysis of untargeted serum metabolomics from patient and healthy controls.

(C) Proteomics profiling using absolute protein quantification in human $MCUR1^{-/-}$ fibroblasts, and engineered Hela cells with shRNA knockdown of MCUR1. The Volcano plot shows

significantly different proteins between control and MCUR1 deficient cells with *p* values below 0.05. MCUR1 was not identified either in control or in patient (false negative), while CCDC90B was identified only in control (FDR 0.05, S0 0.1).
(D) Pathway enrichment analysis of whole cell proteomics from (c). Pathways with positive normalized enrichment score that are significantly enriched with *p* values below 0.05 and *q* values below 0.25 in MCUR1 deficient proteomes are coloured in yellow, while downregulated ones are indicated in blue.
(E) Analysis of MCUR1 protein level in whole-cell lysates from controls and patient fibroblasts compared to patient fibroblasts stably expressing MCUR1 wildtype full-length (rescue). Actin is used as loading control.
(F) Cell migration scratch wound healing assay. Controls, patient-derived fibroblasts, and MCUR1 wildtype rescue of patient-derived fibroblasts were grown in minimal essential media supplemented with serum and uridine after scratch generation. Cell migration was monitored by bright light microscopy in combination with digital image acquisition and data quantification at 0, 12, 24, 36, and 48 hours.
(G) Quantification of cell migration in cells grown as in (F). Data represent mean ± SD (*N*= 3 biologically independent experiments.

SUPPLEMENTARY FIGURE LEGENDS

Fig. S1. MCUR1 deficiency does not impair mt-Ca^{2+} uptake in human cells.
(A) Immunoblot analysis of MCUR1 protein level in whole-cell lysates from HeLa cells stably expressing a mitochondria-targeted aequorin (mt-AEQ) and either an empty lentiviral vector (pLKO) or MCUR1-targeted shRNAs. ß-actin is used as loading control; the arrow indicates the MCUR1-specific band.
(B) Average traces and quantification of mt-Ca^{2+} transients in response to histamine (His) stimulation in control and shMCUR1 HeLa mt-AEQ cells (*N*> 5 biologically independent experiments).
(C) Average traces and quantification of mt-Ca^{2+} uptake in digitonin-permeabilized controls and patient skin fibroblasts in presence of TMPD (0.5 mM)/ ascorbate (2 mM) as respiratory substrates.
(D) Average traces of mt-Ca^{2+} buffering capacity in digitonin-permeabilized controls and patient skin fibroblasts in presence of glutamate (10 mM) and malate (2 mM) as respiratory substrates, upon multiple Ca^{2+} spikes.

Fig. S2. MCUR1 deficiency does not alter MCUC stability and assembly in human cells.
(A) Protein levels of MCUC components in whole-cell lysates from controls and patient skin fibroblasts relative to ß-actin as loading control.
(B) Immunoblot analysis of MCUC subunits in whole-cell lysates from control and shMCUR1 HeLa cells. ß-actin is used as loading control (*N*= 3 biologically independent experiments).
(C) BN-PAGE analysis of MCUC assembly in mitochondria isolated from controls and P1 skin fibroblasts.
(D) BN-PAGE analysis of MCUC in mitochondria isolated from pLKO and shMCUR1 HeLa cells (*N*= 3 biologically independent experiments).

Fig. S3. Mitochondrial bioenergetics in patient fibroblasts and shMCUR1 HeLa cells.

(A) Measurements of mitochondrial respiration in intact patient and control fibroblasts (C1, C2). (*Left*) Average oxygen consumption rate (OCR) kinetics and (*right*) quantification of basal (State II), non-ADP-stimulated (State IV_o) and CCCP-stimulated (State III_u) respiration in response to oligomycin A (O, 1.5 μM) and CCCP (C, 1 μM). Rotenone/antimycin A (R, 2 uM; AA, 4 μM) are used to block RCCI and RCCIII-driven respiration. Data are normalized by total DNA content (*N*= 3 biologically independent experiments with more than 4 technical replicates for each condition).
Measurements of RCCI-dependent (**B**) and RCCII-dependent (**C**) OCR in digitonin-permeabilized patient and control fibroblasts. (*Left*) Average OCR kinetics and (*right*) quantification of basal (State II), ADP-stimulated (State III), non-ADP-stimulated (State IV_o) and CCCP-stimulated (State III_u) respiration in response to ADP (4 mM), oligomycin A (O, 1.5 μM), and CCCP (C, 15 μM) and in presence of (B) a-ketoglutarate (10 mM)/ malate (10 mM) or (C) succinate (10 mM)/rotenone (2 μM) as respiratory substrates. Rotenone (2 μM) and antimycin A (4 μM) are used as RCCI and RCCIII inhibitors, respectively. Data are normalized by total DNA content (*N*= 3 biologically independent experiments, with more than 4 technical replicates for each condition).
(D) Measurements of mitochondrial respiration in intact HeLa cells expressing either pLKO or sh1. (*Left*) Average oxygen consumption rate (OCR) kinetics and (*right*) quantification of basal (State II), non-ADP-stimulated (State IV_o) and CCCP-stimulated (State III_u) respiration in response to oligomycin A (O, 1.5 μM) and CCCP (C, 1 μM). Rotenone/antimycin A (R, 2 uM; AA, 4 μM) are used to block RCCI and RCCIII-driven respiration. Data are normalized by total DNA content (*N*= 3 biologically independent experiments, with more than 4 technical replicates).

Fig. S4. Loss of MCUR1 does not affect RCC level or assembly.
(A) Immunoblot analysis of individual RCC subunits in whole-cell lysates from control and sh-MCUR1 HeLa cells (*N*= 3 biologically independent experiments). ß-actin is used as loading control.
(B) BN-PAGE analysis RCC assembly in mitochondria isolated from control and shMCUR1 HeLa cells (*N*= 3 biologically independent experiments).
(C) BN-PAGE analysis RCC assembly in mitochondria isolated from controls and patient fibroblasts (*N*= 3 biologically independent experiments).

Fig. S5. MCUR1 is not required for respiratory growth in *S. cerevisiae*.
(A) Deletion of *FMP32* (*fmp32*Δ) does not result in a growth phenotype on agar plates supplemented with either glucose (YPD) or lactic acid (YPL) and glycerol (YPG) as fermentable and non-fermentable substrates, respectively, when incubated at 24°C, 30°C or 37°C. *FMP32* was deleted by homologous recombination with two different selection cassettes (HYG, hygromycin; KAN, kanamycin) in two different wild type (WT) yeast strains (YPH499 and BY4742). Data are representative of two independent experiments**.**
(B) Growth analysis of WT and *fmp32*Δ strains in liquid YPD or YPL media at 30°C (mean ± SEM, *N*=4 biologically independent experiments).

Fig. S6. MCUR1 and its paralog CCDC90B form a hetero-oligomeric complex.
(A) Generation of Flp-In™ 293 T-Rex cells expressing a C-terminally tagged MCUR1-His_6-HA-StrepII at near-endogenous level upon tetracycline-dependent induction. Immunoblot analysis of tagged MCUR1 in whole-cell lysates before (-Tet) and after (+Tet) induction with tetracycline.

(B) MCUR1-His_6-HA-StrepII is enriched in mitochondria. Analysis of whole-cell (WCL), nuclear (N), cytosolic (C), and mitochondrial (M) fractions isolated from Flp-In™ 293 T-Rex cells after tetracycline induction. Actin, ATP5a, and lamin A/C are used as positive controls for cytosolic, mitochondrial and nuclear proteins.
(C) MCUR1-His_6-HA-StrepII is an integral mitochondrial membrane protein. Immunoblot analysis of mitochondrial soluble (S) and membrane pellet (P) fractions isolated from tetracycline-induced Flp-In™ 293 T-Rex cells by alkaline carbonate extraction at pH 10 and pH 11. ATP5a and VDAC (membrane associated and membrane spanning proteins, respectively) are used as positive controls.
(D) Analysis of protein topology by proteinase K (PK) treatment of mitochondria isolated from tetracycline-induced Flp-In™ 293 T-Rex cells. TOM20, TIM23, and cyclophilin F (Cyc F) were used as controls for integral mitochondrial outer membrane, inner membrane and soluble matrix targeted proteins, respectively. T, triton (1%); Dig., digitonin.
(E) Volcano plot of mitochondrial protein enrichments by tandem affinity purifications (TAP) from lysates of Flp-In™ 293 T-Rex cells expressing tagged MCUR1 as a bait over parental Flp-In™ 293 T-Rex cells (Ctrl, control), plotted against corresponding *p* values. Binding partners were defined using a two-tailed Student t-test with a permutation-based false discovery rate (FDR) of 0.05 as a threshold. Bait-specific interactors and background interactors are indicated by red and blue dots, respectively. Black dots indicate components of MCUC.
(F) MCUR1 and CCDC90B form a protein complex on BN-PAGE analysis of mitochondrial fractions from control and sh90A HeLa cells (*N*=3 biologically independent experiments). ATP5a is used as a loading control.
(G) Protein expression and quantification of CCDC90B protein level in whole-cell lysates from HeLa cells infected with either an empty lentiviral vector (pLKO, control) or a shRNA against MCUR1, relative to ß-actin as loading control (*N*= 4 biologically independent experiments).

Fig. S7. Evolutionary profile of MCUR1 and CCDC90B
Phylogenetic distribution of MCUR1 and CCDC90B homologs across 247 eukaryotes. The phylogenetic tree was reconstructed using the phylogenetic tree generator (https://phylot.biobyte.de/) and visualized using iTOL (https://itol.embl.de/). Homologs of human MCUR1 and CCDC90B were retrieved from ProtPhylo using OrthoMCL with more than 0% match length and inflation index of 1.1 for orthology assignment.

Fig. S8. Effect of Sp-MCUR1 knockout on growth in presence of different nitrogen sources.
Growth of prototrophic wild-type (WT) and Sp-MCUR1 knockout *S. pombe* cells in minimal media with either arginine (**A**) or glutamate (**B**) or as sole nitrogen sources.
(C) Rescue of growth defect by supplementation of glutamate.

METHODS

Genetic testing
The patient provided written informed consent for participation in the study. The study was approved by the local ethics committee and was conducted in accordance with the ethical principles of the Declaration of Helsinki. After obtaining patient consent, total genomic DNA was extracted from peripheral blood leucocytes of the patient and subjected to whole exome

analysis**.** Coding regions were enriched using a SureSelect Human All Exon V5 kit (Agilent) followed by sequencing as 100-bp paired-end runs on an Illumina HiSeq2500. Reads were aligned to the human reference genome (UCSC Genome Browser build hg19) using Burrows-Wheeler Aligner (v.0.7.5a) and single-nucleotide variants and small insertions and deletions (indels) were detected with SAMtools (version 0.1.19). For segregation analysis Sanger sequencing was performed in all siblings using DNA extracted from peripheral blood leucocytes or buccal epithelial cells.

Cell lines

All mammalian cells were grown in high-glucose Dulbecco's modified Eagle's medium (DMEM) supplemented with 10% FBS at 37ºC and 5% CO_2. HeLa cells stably expressing a wild-type mitochondrial matrix-targeted GFP-aequorin (mt-AEQ) were grown in presence of 100 µg/ml geneticin (Arduino et al., 2017). Primary human skin fibroblasts were grown in presence of 0.2 mM uridine. Primary skin fibroblasts stably expressing wild-type human MCUR1 and mt-AEQ from the pLX304 lentiviral vector were generated by transduction, as previously described in Wettmarshausen & Perocchi (2017), and grown in presence of 0.2 mM uridine and 10 ug/mL blasticidin. HeLa mt-AEQ cells stably expressing either the lentiviral empty vector pLKO or a pLKO vector expressing sh-RNAs targeting human MCUR1 (sh1, TRCN0000134711; sh2, TRCN0000134319; sh3, TRCN0000135627; sh4, TRCN0000136480; sh5, TCRN0000137294) were generated as previously described (Perocchi et al., 2010) and grown in presence of 2 ug/mL puromycin. Lentivirus production and infection were performed according to guidelines from the Broad RNAi Consortium and infected cell lines were selected 48 hr post-transduction with the respective selection markers. Primary control skin fibroblasts were kindly provided Prof. Vincent Bonifati (Erasmus University Medical Center). Parental Flp-In™ 293 T-Rex cells were cultured in presence of 15 µg/mL blasticidin and 100 µg/mL Zeozin. Flp-In™ 293 T-Rex cells stably expressing a C-terminal $StrepII_2$-HA-His_6-tagged MCUR1 under the control of a tetracycline-regulated CMV/$TetO_2$ promoter were grown in presence of 15ug/mL blasticidin and 100ug/mL hygromycin.

SDS/BN-PAGE and immunoblotting

Immunoblot analyses were performed with the following antibodies: MCU (Sigma Aldrich, HPA01648), anti-ATP5A (Abcam, MS507), NDUFB8 (Abcam, ab110242), SDHA (Abcam, ab14715), UQCRC2 (Abcam, ab14745), MTCO II (Abcam, ab110258), EMRE (Santa Cruz, sc-86337), MCUB (Santa Cruz, sc-163985), MCUR1 (Thermo Fisher, PA5-32164), CCDC90B (Sigma Aldrich, HPA011931),TIM23 (BD Bioscience, 611222), TOM20 (Abcam, ab56783), Cyclophilin D (Abcam, ab110324), MICU1 (Atlas Antibody, HPA037479), MICU2 (Sigma Aldrich, HPA045511), Actin (Sigma Aldrich, A2228), HA (BioLegend, MMS-101R), VDAC1/Porin (Abcam, ab14734), Lamin A/C (abcam, ab238303). BN-PAGE was performed as previously described (Wettmarshausen & Perocchi, 2017). Briefly, crude mitochondria were solubilized for 10 min on ice in 1xNativePAGE™ sample buffer containing 1% (w/v) digitonin and after a centrifugation step at 20,000 x *g* for 30 min at 4ºC, the supernatant was mixed with 0.25% of NativePAGE™ G-250 sample additive and resolved on a 3-12% gradient NativePAGE™ Novex Bis-Tris gel according to the manufacturer's protocol. Proteins were transferred onto PVDF membranes by electrophoretic wet transfer overnight at 40V, 4ºC. After transfer, proteins were fixed on the membrane by incubating in 8% acetic acid for 15 min at room temperature for immunoblot analyses.

Mitochondrial bioenergetics in intact and permeabilized cells

Glycolytic and mitochondrial respiratory activities were assessed by microplate-based respirometry using a Seahorse Extracellular Flux (XF) Analyzer (Agilent Technologies, Santa Clara, USA) as previously described (Wettmarshausen & Perocchi, 2019). Briefly, cells were seeded on a Seahorse XF cell culture 96-well plate in growth media and incubated overnight at 37ºC and 5% CO_2. For measurements of oxygen consumption rate (OCR) and extracellular acidification rate (ECAR) in intact cells, the growth medium was replaced with either mito-stress assay (MSA) medium containing pyruvate (1 mM), L-glutamine (2 mM), and glucose (10 mM) or glycolysis assay medium with L-glutamine (2mM). Cells were then incubated at 37ºC and 5% CO_2 for 1 hour. For measurements of For OCR measurements in permeabilized cells, cells were washed with PBS and incubated for 5 min in a mito-assay medium (MAS) containing d-mannitol (200 mM), d-sucrose (70 mM), 2.5 $MgCl_2$ (5 mM), KH_2PO_4 (10mM), HEPES-KOH (2 mM), EGTA-KOH (1 mM), 0.5% fatty-acid free BSA, and digitonin (60 µM for HeLa cells and 25 µM for primary skin fibroblasts) to selectively permeabilize the plasma membrane. Cells were then washed with MAS and OCR was measured in MAS containing respiratory substrates. OCR and ECAR measurements were normalized to cell number by quantifying total DNA with the CyQUANT Cell Proliferation Assay Kit.

Isolation of crude mitochondria from cultured cells

Crude mitochondria were isolated from cultured cells as previously described (Wettmarshausen & Perocchi, 2017). Briefly, cells were grown to confluency, washed three times with PBS, scraped down and resuspended in PBS. After 5 min of centrifugation at 600 x *g*, 4ºC, the cell pellet was resuspended in ice cold isolation buffer (IB: 220 mM d-mannitol, 70 mM d-sucrose, 5 mM HEPES-KOH pH 7.4, 1 mM EGTA-KOH pH 7.4, 0.5% fatty acid-free BSA, protease inhibitors). The plasma membrane was permeabilized by nitrogen cavitation at 600 psi for 10 min at 4ºC. The whole cell homogenate was then centrifuged at 600 x *g* for 10 min at 4ºC and the pellet (including the nuclei fraction) was saved for immunoblotting. The supernatant was transferred into new tubes and centrifuged at 8000 x *g* for 10 min at 4ºC. The supernatant (corresponding to the cytosolic fraction) was saved for immunoblotting and the resulting pellet containing crude mitochondria was resuspended in IB for further analyses.

Measurements of mitochondrial calcium uptake in intact human cells

Mitochondrial Ca^{2+} uptake was measured in intact HeLa cells and primary skin fibroblasts expressing mt-AEQ as previously described (Arduino et al., 2017). Briefly, cells were seeded in white 96-well plates in growth medium without selection marker and after 24 hours, mt-AEQ was reconstituted with 2 uM native coelenterazine for 2 hours at 37ºC and 5% CO_2. AEQ-based, Ca^{2+}-dependent light kinetics were measured upon stimulation with histamine (100 uM). Light emission was measured in a luminescence counter (MicroBeta2 LumiJET Microplate Counter, PerkinElmer) at 469 nm every 0.1 s. At the end of each experiment, cells were lysed with a solution containing 0.5% Triton X-100 and 10 mM $CaCl_2$ to release all the residual aequorin counts. Quantification of mt-Ca^{2+} concentration was performed as described also as previously described.

Measurements of mitochondrial calcium uptake in digitonin-permeabilized human cells

Mitochondrial Ca^{2+} uptake was measured in permeabilized HeLa cells and primary skin fibroblasts expressing mt-AEQ as previously described (Wettmarshausen & Perocchi, 2017). Briefly, cells were harvested at a density of 500,000 cells/mL in growth medium containing 20 mM HEPES-NaOH, pH 7.4. AEQ was reconstituted with 3 uM native coelenterazine for 2 hours at room temperature and the cell pellet was then incubated in an extracellular-like buffer (145 mM NaCl, 5 mM KCl, 1 mM $MgCl_2$, 10 mM glucose, 10mM HEPES and 500 uM EGTA pH 7.4/NaOH) containing 200 nM thapsigargin for 20 min at room temperature. Cells were re-suspended in an intracellular-like buffer (140 mM KCl, 1 mM KH_2PO_4/K_2HPO_4, 1 mM $MgCl_2$, 1 mM ATP/$MgCl_2$, 20 mM HEPES and 100 uM EGTA pH 7.2/KOH) supplemented with respiratory substrates. Cells were permeabilized with either 60 uM (HeLa cells) or 25 µM (human skin fibroblasts) digitonin for 5 min and re-suspended in intracellular-like buffer at a density of 900 cells/uL. Then, 90 uL of cell suspension was dispensed into a white 96-well plate and Ca^{2+}-stimulated light signal was recorded at 469 nm every 0.1 s using a luminescence counter (MicroBeta2 LumiJET Microplate Counter, PerkinElmer). At the end of each experiment, cells were lysed with a solution containing 0.5% Triton X-100 and 10 mM $CaCl_2$ to release all the residual aequorin counts. Quantification of mt-Ca^{2+} concentration was performed as described in Arduino et al. (2017). Measurement of mt-Ca^{2+} buffering capacity in digitonin permeabilized human cells was performed as previously described using Calcium Green-5N Hexapotassium Salt, cell impermeant. Calcium Green-5N fluorescence (excitation 506 nm, emission 531 nm) was monitored every 2 s at room temperature using a CLARIOstar microplate reader (BMG Labtech) upon injection of $CaCl_2$. The MCU inhibitor Ru360 (10 uM) was used as a positive control.

Stable protein expression in Flp-In™ 293 T-Rex cells

Flp-In™ 293 T-Rex cells stably expressing a C-terminal StrepII$_2$-HA-His$_6$-tagged MCUR1 under the control of a tetracycline-regulated CMV/TetO$_2$ promoter were generated as previously described (Delgado de la Herran et al., 2024). First, the open reading frame (ORF) of MCUR1 was cloned into the pcDNA5/FRT/TO Flp-In expression vector, in frame with a C-terminal StrepII$_2$-HA-His$_6$-tag. Flp-In™ 293 T-Rex cells contain a single integrated flippase (Flp) recognition (FRT) site and stably express the *lacZ-ZeocinTM* fusion gene (pFRT/*lac*Zeo) and the tetracycline repressor (pcDNA6/TR). Co-transfection of Flp-In™ 293 T-Rex cells with the Flp-In™ expression vector and the Flp recombinase vector pOG44 results in a targeted integration of MCUR1 at a single transcriptionally active genomic locus that is the same in each cell. Briefly, cells were seeded in 6-well plates without antibiotics and transfected with 80 ng of the Flp-In™ expression vector and 720 ng of pOG44 using X-tremeGENE™ HP DNA according to manufacturer's protocol. Stable transfectants were selected and maintained in growth medium containing blasticidin (15ug/mL) and hygromycin (100ug/mL). The expression of the tagged bait protein was induced with 1 µg/mL tetracycline in media without antibiotics. After 24 hours, cells were washed three times with PBS and the cell pellet was collected at 600 x *g* for 10 min at 4°C and stored at -80°C till further use.

Tandem affinity purification

A cell pellet containing ~90 x 10^6 cells was re-suspended in 2 mL lysis buffer (50mM HEPES-KOH pH7.4, 150mM KCL, 5mM EGTA, 5% glycerol, 3% digitonin, protease inhibitors), incubated for 30 min at 4 °C on a rotating shaker, and centrifuged at 10 000 x *g* for 5 min at 4 °C. The supernatant was mixed with HEPES-KOH pH 8 (12.5 mM) and avidin (10 uM) and incubated for 20 min at room temperature on a rotating shaker. The resin (150 uL streptavidin) was washed three times with 500 µL washing buffer (WB: 50 mM HEPES-KOH

pH 7.4, 150 mM KCl, 5 mM EGTA, 5% glycerol, 0.02% digitonin), incubated with the supernatant for 45 min at 4 °C on a rotating shaker, and washed again three times with WB. Next, the resin was incubated with 250 µL of elution buffer (EB: 50 mM HEPES-KOH pH 8, 150 mM KCl, 5 mM EGTA, 5% glycerol**,** 10 mM biotin) for 5 min at room temperature and the eluate was collected with a quick spin. The same procedure was repeated three times and the eluates were then combined and incubated with 50 uL of Ni-NTA resin for 45 min at 4 °C on a rotating shaker. Any unbound fraction was removed by washing three times with 500 µL WB. For SDS-PAGE analysis, the resin was resuspended in 1x Laemmli, whereas for LC-MS/MS analysis the resin was washed three times with digitonin-free WB followed by incubation with 35 µL RapiGest for 10 min at room temperature. Five volumes of ice-cold acetone were added to the eluate, the sample was vortexed thoroughly for 10 sec and incubated overnight at -20°C. The sample was centrifuged at 20 000 x g for 30 min at 4 °C and the pellet was stored at -80 °C for LC-MS/MS analysis.

Sample preparation for mass spectrometry analysis

Eluates were resuspended in 50 µl denaturation buffer (6 M urea, 2 M thiourea, 10 mM HEPES pH 8.0, 10 mM DTT) for 30 min at RT before adding alkylation agent (55 mM iodoacetamide) and incubating at RT in the dark for 20 min. Proteins were digested at RT for 3 hrs by adding LysC at 1:100 ratio of enzyme:protein, before diluting the sample with 50 mM ammonium bicarbonate to reach urea concentration of 2M. Subsequently, samples were digested at RT overnight by adding Trypsin at 1:100 ratio of enzyme:protein. The next day, the digestion was stopped by acidifying the sample with 10 µL of 10% TFA and the final peptides were cleaned up using SDB-RPS StageTips as described in (Kulak et al., 2014).

Whole cell proteome analysis

Whole proteome of Hela cells and human skin fibroblasts was analyzed by LC-MS/MS mass spectrometry. The cells were lysed by scraping them in a lysis buffer containing 1% sodium deoxycholate, 10 mM of the reducing agent tris(2-carboxyethyl)phosphine (TCEP) and 40 mM of the alkylating agent 2-chloroacetamide (CAA),chloroacetamide, an optimized reaction mix that allows reduction and alkylation to be performed as a single step (Kulak et al 2014). The lysate was boiled and sonicated using a Bioruptor system (10 cycles, 30 sec on/off; Diagenode, Belgium), acetone precipitated and then digested as described above. Samples (20 ug) were digested overnight with LysC and Trypsin in a 1:40 ratio and desalted using SDB-RPS StageTips.

LC-MS/MS analysis

MS analysis was performed using Q Exactive HF mass spectrometers (Thermo Fisher Scientific, Bremen, Germany) coupled on-line to a nanoflow UHPLC instrument (Easy1000 nLC, Thermo Fisher Scientific). Peptides were separated on a 50 cm long (75 µm inner diameter) column packed in-house with ReproSil-Pur C18-AQ 1.9 µm resin (Dr. Maisch GmbH, Ammerbuch, Germany). Column temperature was kept at 50 °C. Peptides were loaded with buffer A (0.1% (v/v) formic acid) and eluted with a nonlinear gradient of 5-60% buffer B (0.1% (v/v) formic acid, 80% (v/v) acetonitrile) at a flow rate of 250 nl/min. Peptide separation was achieved by 120 min gradients for both whole proteomes and pulldowns. For pulldowns, the survey scans (300-1650 m/z, target value = 3E6, maximum ion injection times = 20 ms) were acquired at a resolution of 60,000 followed by higher-energy collisional dissociation (HCD) based fragmentation (normalized collision energy = 27) of up to 15 dynamically chosen, most abundant precursor ions. The MS/MS scans were acquired at a

resolution of 15000 (target value = 1E5, maximum ion injection times = 60 ms). Repeated sequencing of peptides was minimized by excluding the selected peptide candidates for 20 seconds. For whole proteome analysis the survey scans were acquired at a resolution of 120,000, the MS/MS scans at a resolution of 15000 and a dynamic exclusion of 30 seconds.

MS data processing

Interactome data were analysed using the MaxQuant software package 1.5.5.2 (Cox & Mann, 2008). The false discovery rate (FDR) cut-off was set to 1% for protein and peptide spectrum matches. Peptides were required to have a minimum length of 7 amino acids and a maximum mass of 4600 Da. MaxQuant was used to score fragmentation scans for identification based on a search with an initial allowed mass deviation of the precursor ion of a maximum of 4.5 ppm after time-dependent mass calibration. The allowed fragment mass deviation was 20 ppm. Fragmentation spectra were identified using the UniprotKB *Homo sapiens* database with the Andromeda search engine (Cox et al., 2011). Carbamidomethylation of cysteine was set as fixed modification and N-terminal protein acetylation as well as methionine oxidation as variable modifications. Both 'label-free quantification (MaxLFQ)' with a minimum ratio count of 1 and 'match between runs' with standard settings were enabled (Cox et al., 2014). Fibroblasts and HeLa proteome data were analysed using the MaxQuant version 1.6.0.12 with the same parameters. The mass spectrometric data have been deposited via PRIDE (Vizcaíno et al., 2013) to the ProteomeXchange Consortium (http://proteomecentral.proteomexchange.org) under the accession number PXD017460.

MS data analysis and visualization

Basic data handling, normalization, statistics, and annotation enrichment analysis was performed with the Perseus software package (Tyanova et al., 2016). To generate the list of interactors of the three baits analysed, we used the MaxLFQ, MaxQuant's label-free quantification (LFQ) algorithm (Cox et al., 2014). ProteinGroups were filtered removing hits to the reverse decoy database and proteins only identified by modified peptides. Differentially expressed proteins were identified by two-tailed Student t-test using the volcano plot option of Perseus.

Analysis of mitochondrial protein topology

The topology of mitochondrial proteins was assessed by proteinase K (PK) protection assay on freshly isolated crude mitochondria as previously described (Wettmarshausen & Perocchi, 2017). Briefly, mitochondria were incubated for 15 min at room temperature in IB buffer containing increasing concentrations of digitonin or 1% TritonX-100 and 100ug/ml PK. PK was inactivated by incubation with 5 mM PMSF on ice for 10 min. Samples were then mixed with Laemmli buffer containing 10% 2-mercaptoethanol for immunoblot analysis. Alkaline carbonate extraction was performed by incubating crude mitochondria with 0.1 M Na_2CO_3 at pH 10 and pH 11 for 30 min on ice. Samples were then centrifuged at 45,000 x g for 10 min at 4°C and the pellets were resuspended in Laemmli buffer containing 10% 2-mercaptoethanol for immunoblot analysis. Supernatants were mixed with 100% TCA, incubated overnight at -20°C, and then centrifuged at 16,000 x g for 25 min at 4°C. Pellets were then washed twice with cold acetone, air-dried for 30 min at room temperature and resuspended in Laemmli buffer for immunoblot analysis.

***Saccharomyces cerevisiae* strains and growth measurements**

FMP32 was deleted in BY4742 and YPH499 wild type *S. cerevisiae* strains by homologous recombination using hygromycin or kanamycin cassettes. Yeast transformation was performed by lithium acetate method and transformants were selected on YPD (1% yeast extract, 2% peptone, and 2% glucose) plates containing either hygromycin (200µg/mL) or G418 (500µg/mL), respectively. Successful deletion of *FMP32* in individual clones was confirmed by isolation of genomic DNA and subsequent PCR using the following primer pairs: SacFmp32p (5´- CCC GAG CTC TT ACC GTC TCA ATT TCA CAA G -3´) and KanB (5´- CTG CAG CGA GGA GCC GTA AT -3´) and SacFpm32p and Fmp32Stop132Eco (5´- CCC GAA TTC CTA TTT GGT AAT AAC AAC CCT TAG – 3´). The former primer pair was used to confirm the successful deletion and the latter to exclude the presence of the wild type copy of the gene. Genomic DNAs isolated from wild type BY4742 strain and *Dfmp32:KAN* obtained from from the Saccharomyces Genome Deletion Project (http://www-sequence.stanford.edu/group/yeast deletion project/deletions3.html) served as controls for PCR reactions. For growth assays in liquid media, yeast cultures were grown at 30°C overnight in YPD media, diluted to an OD of 0.1 and then grown in black, gas-permeable Lumox 96-well plates. Absorbance was measured at 600 nm and at intervals of 340 s using a CLARIOstar microplate reader (BMG Labtech) for 24 hours at 30°C. For growth assays on agar plates, yeast cultures were grown at 30°C overnight in YPGal media (1% yeast extract, 2% peptone, and 2% galactose), diluted in the morning to an OD of 0.1 in fresh YPGal medium and grown at 30°C till they reached an OD of 0.5. Cells were harvested, washed with water and spotted on agar plates containing different carbon sources (YPD; YPG, 3% glycerol; YPL, 2% lactic acid) following a 10-fold serial dilution and incubated at 24 °C, 30 °C or 37 °C.

***Schizosaccharomyces pombe* strains and growth measurements**

Single and double knockout of SPAC2C4.09 (Sp-MCUR1) and SPAC3H1.08c (Sp-CCDC90B) in the prototroph *S. pombe* 972 h strain were constructed by homologous recombination by lithium acetate transformation of PCR products containing 500 bp of targeting homology using *KanMX6* and natMX6, respectively, as selection markers as described previously (Bähler et al., 1998). For expression of human MCUR1, CCDC90B, or both, codon-optimized sequences were integrated into the chromosomal loci of SPAC2C4.09 and SPAC3H1.08c and expressed under the control from their endogenous promoters, respectively. Insertions of *MCUR1* and *CCDC90B* were generated by replacing the deletion cassettes SPAC2C4.09::KanMX6 and SPAC3H1.08c::natMX6 individually with *MCUR1*::hygMX and *CCDC90B*::kanMX by homologous recombination. The correct genomic integration and expression of the human homologs were confirmed by diagnostics PCR using genomic DNA and quantitative PCR of total RNA with gene-specific primers (RT-qPCR), respectively. Yeast extract with supplements (YES) media containing 0.5 % (w/v) yeast extract, 3.0 % (w/v) glucose, 225 mg/l adenine, 225 mg/l histidine, 225 mg/l leucine, 225 mg/l uracil, 225 mg/l lysine hydrochloride) was used for liquid culture, unless specified otherwise. Deletion strains were selected on YES plates containing 100 mg/l G418, 100 mg/ hygromycin, and 50 mg/ml nourseothricin, respectively. Liquid growth assays were conducted as descripted for *S. cerevisiae* strains using minimal media at 30 °C with either ammonium sulphate, arginine, proline, or glutamate as sole nitrogen source.

Unlabelled and N^{15} labelled metabolomics of *S. pombe*

Double Sp-MCUR1 and Sp-CCDC90B and wildtype *S. Pombe* strains were grown for ~24 h till mid-log phase in minimal media at 30 °C, the pellet was washed two times with PBS and

resuspended in Yeast Nitrogen Base (YNB) media without amino acids and ammonium with either ^{15}N labelled or unlabelled ammonium sulphate. After 12-16 hours of growth cells were collected, washed three times with water and the pellet was snap frozen in liquid nitrogen and stored at -80°C until use. Pool size or stable isotope incorporation was quantified by integration and validated by standards. Each trace was mapped to a HMDB ID, which allowed for pathway enrichment analysis by metaboanalyst.

Scratch assay

All cell lines were seeded in 12-well plates and cultured in DMEM with 10% FBS and 2µM uridine until 70% confluency. Then a scratch was made in each well using a 200µl sterile pipette tip of about 50 µm. Cells were washed twice with PBS, in order to remove the debris and smooth the edge of the scratch, and incubated in MEM with 10% FBS and 2µM uridine. Images were acquired every 12h up to 24h after scratch generation using the EVOS XL core (AMEX 1000R, life technologies). Scratch reduction was determined counting of the cells that cross into the scratch area from their reference point at time 0 and normalized on the number of cells at both the sides of the scratch by Image Pro-Plus 10 software (Media Cybernetics).

Data analysis

Data are represented as mean ± SEM and the statistical analysis of each experiment is described in the figure legends including the statistical tests used and the exact value of biological replicates. For each biological replicate experiment at least 3 technical replicates were used for quantification and data analysis. Normal distribution was tested by Shapiro-Wilk normality test. Statistical analyses were performed using GraphPad Prism (GraphPad Software, version 7).

Acknowledgements

We acknowledge Dr. Cecilia Garcia-Perez, Dr. Alexandros A Pittis, and Dr. Fabian Hosp for experimental and computational support. FP group was supported by the Munich Center for Systems Neurology (SyNergy EXC 2145 /ID 390857198) and the Initiative and Network Fund of the Helmholtz Association; work in DM group is supported by Deutsche Forschungsgemeinschaft (grants MO1944/1-2 and MO1944/2-1). DM acknowledges the expert technical assistance of Petra Robisch. TBH and HP received funding from the European Commission (Recon4IMD - GAP-101080997).

Author contributions

Conceptualization, F.P. and F.V.F.; Methodology, J.V.F., S.B., M.M., K.L., T.H., M.D., H.P.; Formal Analysis, J.W., F.V.F., S.W., Y.C., R.N.; Visualization, J.V.F., and J. W.; Investigation, J.V.F., J.W., V.G, M.S.F., H.C.D., A.L., K.L.; Resources, F.P., M.M., B.S., D.M.; Writing – Original Draft, F.P. and F.V.F.; Supervision, F.P., M.J., B.S., D.M., M.M.; Funding acquisition: F.P.

Competing interests: The authors declare no competing interests.

Correspondence and requests for materials should be addressed to fabiana.perocchi@tum.de

References

Adlakha, J., Karamichali, I., Sangwallek, J., Deiss, S., Bär, K., Coles, M., Hartmann, M. D., Lupas, A. N., & Hernandez Alvarez, B. (2019). Characterization of MCU-Binding Proteins MCUR1 and CCDC90B - Representatives of a Protein Family Conserved in Prokaryotes and Eukaryotic Organelles. *Structure (London, England□: 1993)*, *27*(3), 464-475.e6. https://doi.org/10.1016/J.STR.2018.11.004

Arduino, D. M., Wettmarshausen, J., Vais, H., Navas-Navarro, P., Cheng, Y., Leimpek, A., Ma, Z., Delrio-Lorenzo, A., Giordano, A., Garcia-Perez, C., Médard, G., Kuster, B., García-Sancho, J., Mokranjac, D., Foskett, J. K., Alonso, M. T., & Perocchi, F. (2017). Systematic Identification of MCU Modulators by Orthogonal Interspecies Chemical Screening. *Molecular Cell*, *67*(4), 711-723.e7. https://doi.org/10.1016/J.MOLCEL.2017.07.019

Bähler, J., Wu, J. Q., Longtine, M. S., Shah, N. G., McKenzie, A., Steever, A. B., Wach, A., Philippsen, P., & Pringle, J. R. (1998). Heterologous modules for efficient and versatile PCR-based gene targeting in Schizosaccharomyces pombe. *Yeast (Chichester, England)*, *14*(10), 943–951. https://doi.org/10.1002/(sici)1097-0061(199807)14:10<943::aid-yea292>3.0.co;2-y

Chaudhuri, D., Artiga, D. J., Abiria, S. A., & Clapham, D. E. (2016). Mitochondrial calcium uniporter regulator 1 (MCUR1) regulates the calcium threshold for the mitochondrial permeability transition. *Proceedings of the National Academy of Sciences of the United States of America*, *113*(13), E1872–E1880. https://doi.org/10.1073/PNAS.1602264113

Cox, J., Hein, M. Y., Luber, C. A., Paron, I., Nagaraj, N., & Mann, M. (2014). Accurate proteome-wide label-free quantification by delayed normalization and maximal peptide ratio extraction, termed MaxLFQ. *Molecular & Cellular Proteomics□: MCP*, *13*(9), 2513–2526. https://doi.org/10.1074/MCP.M113.031591

Cox, J., & Mann, M. (2008). MaxQuant enables high peptide identification rates, individualized p.p.b.-range mass accuracies and proteome-wide protein quantification. *Nature Biotechnology*, *26*(12), 1367–1372. https://doi.org/10.1038/NBT.1511

Cox, J., Neuhauser, N., Michalski, A., Scheltema, R. A., Olsen, J. V., & Mann, M. (2011). Andromeda: a peptide search engine integrated into the MaxQuant environment. *Journal of Proteome Research*, *10*(4), 1794–1805. https://doi.org/10.1021/PR101065J

Delgado de la Herran, H., Vecellio Reane, D., Cheng, Y., Katona, M., Hosp, F., Greotti, E., Wettmarshausen, J., Patron, M., Mohr, H., Prudente de Mello, N., Chudenkova, M., Gorza, M., Walia, S., Feng, M. S. F., Leimpek, A., Mielenz, D., Pellegata, N. S., Langer, T., Hajnóczky, G., … Perocchi, F. (2024). Systematic mapping of mitochondrial calcium

uniporter channel (MCUC)-mediated calcium signaling networks. *EMBO Journal*, *43*(21), 5288–5326. https://doi.org/10.1038/S44318-024-00219-W/SUPPL_FILE/44318_2024_219_MOESM12_ESM.PDF

Garbincius, J. F., & Elrod, J. W. (2021). Mitochondrial calcium exchange in physiology and disease. *Physiological Reviews*, *102*(2), 893. https://doi.org/10.1152/PHYSREV.00041.2020

Jiang, L., Wang, M., Lin, S., Jian, R., Li, X., Chan, J., Dong, G., Fang, H., Robinson, A. E., Aguet, F., Anand, S., Ardlie, K. G., Gabriel, S., Getz, G., Graubert, A., Hadley, K., Handsaker, R. E., Huang, K. H., Kashin, S., … Snyder, M. P. (2020). A Quantitative Proteome Map of the Human Body. *Cell*, *183*(1), 269-283.e19. https://doi.org/10.1016/J.CELL.2020.08.036

Kulak, N. A., Pichler, G., Paron, I., Nagaraj, N., & Mann, M. (2014). Minimal, encapsulated proteomic-sample processing applied to copy-number estimation in eukaryotic cells. *Nature Methods*, *11*(3), 319–324. https://doi.org/10.1038/NMETH.2834

Mallilankaraman, K., Doonan, P., Cárdenas, C., Chandramoorthy, H. C., Müller, M., Miller, R., Hoffman, N. E., Gandhirajan, R. K., Molgó, J., Birnbaum, M. J., Rothberg, B. S., Mak, D. O. D., Foskett, J. K., & Madesh, M. (2012). MICU1 is an essential gatekeeper for mcu-mediated mitochondrial Ca 2+ uptake that regulates cell survival. *Cell*, *151*(3), 630–644. https://doi.org/10.1016/J.CELL.2012.10.011/ATTACHMENT/92302327-F14D-4C77-8DAF-7EB0B1A65A48/MMC2.PDF

Paupe, V., Prudent, J., Dassa, E. P., Rendon, O. Z., & Shoubridge, E. A. (2015). CCDC90A (MCUR1) is a cytochrome c oxidase assembly factor and not a regulator of the mitochondrial calcium uniporter. *Cell Metabolism*, *21*(1), 109–116. https://doi.org/10.1016/J.CMET.2014.12.004

Perocchi, F., Gohil, V. M., Girgis, H. S., Bao, X. R., McCombs, J. E., Palmer, A. E., & Mootha, V. K. (2010). MICU1 encodes a mitochondrial EF hand protein required for Ca(2+) uptake. *Nature*, *467*(7313), 291–296. https://doi.org/10.1038/NATURE09358

Pittis, A. A., Goh, V., Cebrian-Serrano, A., Wettmarshausen, J., Perocchi, F., & Gabaldón, T. (2020). Discovery of EMRE in fungi resolves the true evolutionary history of the mitochondrial calcium uniporter. *Nature Communications 2020 11:1*, *11*(1), 1–10. https://doi.org/10.1038/s41467-020-17705-4

Rallis, C., Codlin, S., & Bähler, J. (2013). TORC1 signaling inhibition by rapamycin and caffeine affect lifespan, global gene expression, and cell proliferation of fission yeast. *Aging Cell*, *12*(4), 563–573. https://doi.org/10.1111/ACEL.12080

Sancak, Y., Markhard, A. L., Kitami, T., Kovács-Bogdán, E., Kamer, K. J., Udeshi, N. D., Carr, S. A., Chaudhuri, D., Clapham, D. E., Li, A. A., Calvo, S. E., Goldberger, O., & Mootha, V. K. (2013). EMRE is an essential component of the mitochondrial calcium uniporter complex. *Science (New York, N.Y.)*, *342*(6164), 1379–1382. https://doi.org/10.1126/SCIENCE.1242993

Tomar, D., Dong, Z., Shanmughapriya, S., Koch, D. A., Thomas, T., Hoffman, N. E., Timbalia, S. A., Goldman, S. J., Breves, S. L., Corbally, D. P., Nemani, N., Fairweather, J. P., Cutri, A. R., Zhang, X., Song, J., Jaña, F., Huang, J., Barrero, C., Rabinowitz, J. E., … Madesh, M. (2016). MCUR1 Is a Scaffold Factor for the MCU Complex Function and Promotes Mitochondrial Bioenergetics. *Cell Reports*, *15*(8), 1673–1685. https://doi.org/10.1016/J.CELREP.2016.04.050

Tyanova, S., Temu, T., Sinitcyn, P., Carlson, A., Hein, M. Y., Geiger, T., Mann, M., & Cox, J. (2016). The Perseus computational platform for comprehensive analysis of (prote)omics data. *Nature Methods*, *13*(9), 731–740. https://doi.org/10.1038/NMETH.3901

Vais, H., Tanis, J. E., Müller, M., Payne, R., Mallilankaraman, K., & Foskett, J. K. (2015). MCUR1, CCDC90A, is a regulator of the mitochondrial calcium uniporter. *Cell Metabolism*, *22*(4), 533–535. https://doi.org/10.1016/j.cmet.2015.09.015

VanderSluis, B., Hess, D. C., Pesyna, C., Krumholz, E. W., Syed, T., Szappanos, B., Nislow, C., Papp, B., Troyanskaya, O. G., Myers, C. L., & Caudy, A. A. (2014). Broad metabolic sensitivity profiling of a prototrophic yeast deletion collection. *Genome Biology*, *15*(4), 1–18. https://doi.org/10.1186/GB-2014-15-4-R64/FIGURES/7

Vizcaíno, J. A., Côté, R. G., Csordas, A., Dianes, J. A., Fabregat, A., Foster, J. M., Griss, J., Alpi, E., Birim, M., Contell, J., O'Kelly, G., Schoenegger, A., Ovelleiro, D., Pérez-Riverol, Y., Reisinger, F., Ríos, D., Wang, R., & Hermjakob, H. (2013). The PRoteomics IDEntifications (PRIDE) database and associated tools: status in 2013. *Nucleic Acids Research*, *41*(Database issue). https://doi.org/10.1093/NAR/GKS1262

Wettmarshausen, J., & Perocchi, F. (2017). Isolation of Functional Mitochondria from Cultured Cells and Mouse Tissues. *Methods in Molecular Biology (Clifton, N.J.)*, *1567*, 15–32. https://doi.org/10.1007/978-1-4939-6824-4_2

Wettmarshausen, J., & Perocchi, F. (2019). Assessing Calcium-Stimulated Mitochondrial Bioenergetics Using the Seahorse XF96 Analyzer. *Methods in Molecular Biology (Clifton, N.J.)*, *1925*, 197–222. https://doi.org/10.1007/978-1-4939-9018-4_18

Zulkifli, M., Neff, J. K., Timbalia, S. A., Garza, N. M., Chen, Y., Watrous, J. D., Murgia, M., Trivedi, P. P., Anderson, S. K., Tomar, D., Nilsson, R., Madesh, M., Jain, M., & Gohil, V. M. (2020). Yeast homologs of human MCUR1 regulate mitochondrial proline metabolism. *Nature Communications 2020 11:1*, *11*(1), 1–15. https://doi.org/10.1038/s41467-020-18704-1

A

Summary of clinical findings of patient	
Clinical phenotype	Early adult onset and progressive neurological symptoms including central oculomotor disturbances, pyramidal tract and cerebellar signs, pathological laughter.
Age of onset	25 years
Family history	Healthy consanguineous parents, 7 healthy siblings
Laboratory findings	Normal blood lactate and cerebrospinal fluid
Brain magnetic resonance	Bilateral hyperintensities in the internal capsule and central brainstem.
Biopsy findings	Normal myohistological investigation and respiratory chain complexes activity in muscle.

B

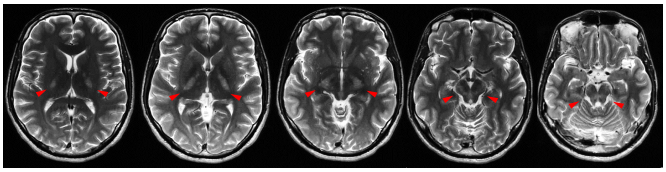

C

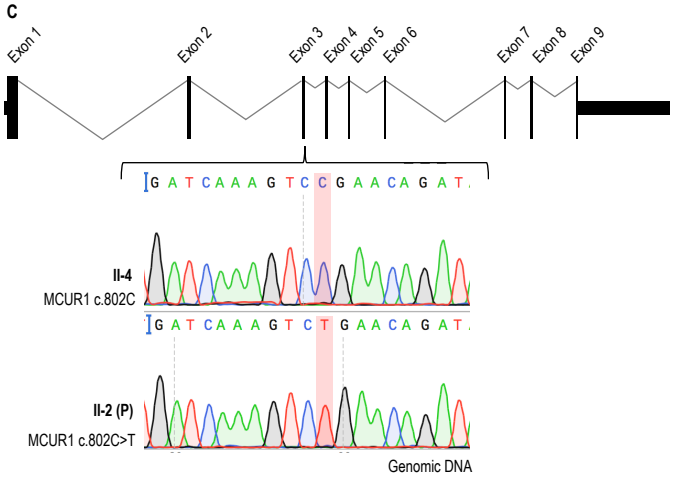

D

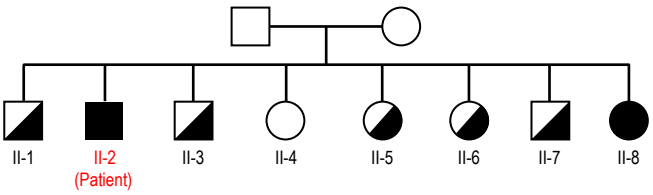

E

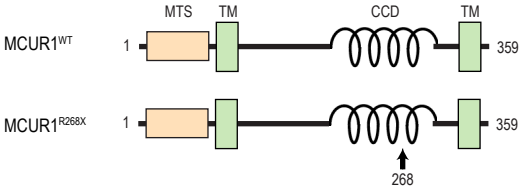

F

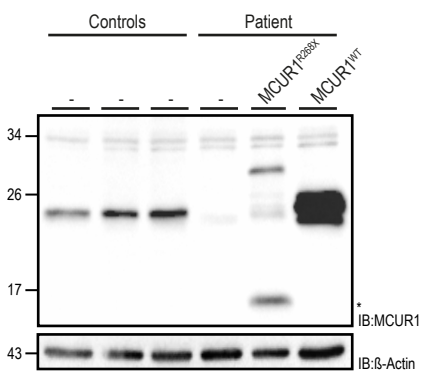

G

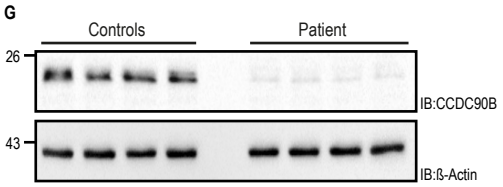

Figure 1

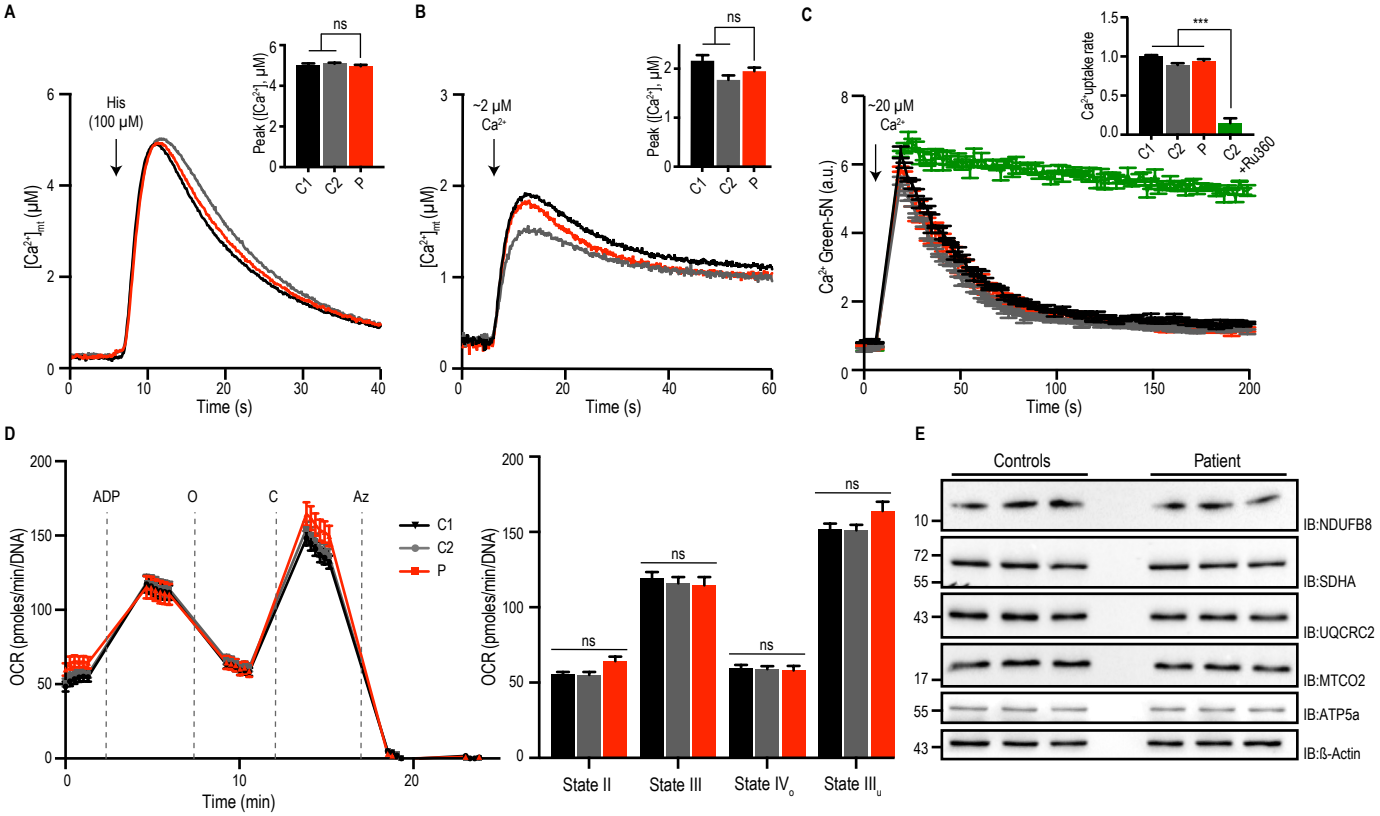
A
His
(100 μM)
[Ca2+]mt (μM)
Time (s)
Peak ([Ca2+], μM)
ns
C1
C2
P
B
~2 μM
Ca2+
[Ca2+]mt (μM)
Time (s)
Peak ([Ca2+], μM)
ns
C
~20 μM
Ca2+
Ca2+ Green-5N (a.u.)
Time (s)
Ca2+uptake rate
***
+Ru360
D
ADP
O
C
Az
OCR (pmoles/min/DNA)
Time (min)
C1
C2
P
State II
State III
State IVo
State IIIu
ns
E
Controls
Patient
IB:NDUFB8
IB:SDHA
IB:UQCRC2
IB:MTCO2
IB:ATP5a
IB:ß-Actin

Figure 2

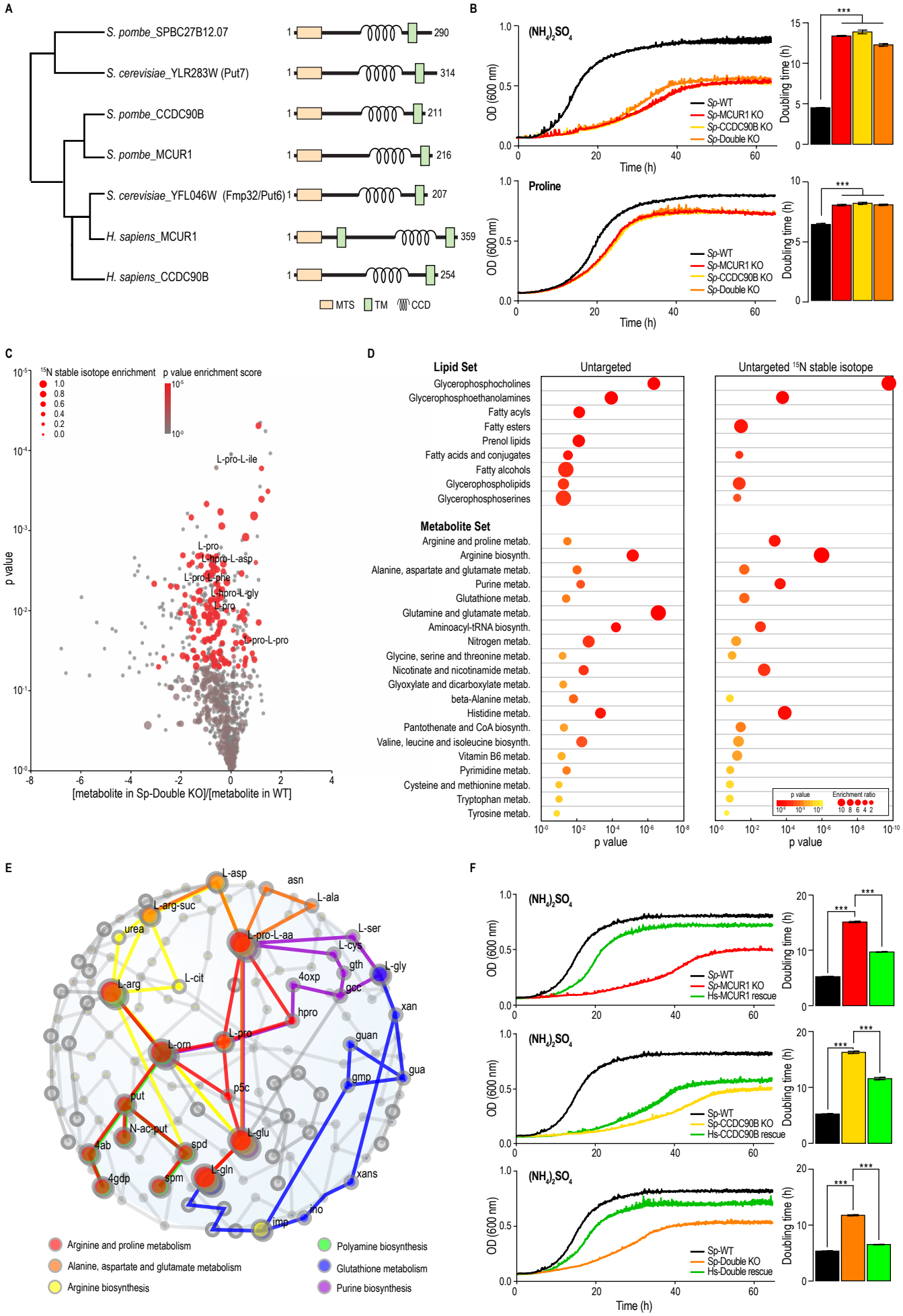
A
S. pombe_SPBC27B12.07
S. cerevisiae_YLR283W (Put7)
S. pombe_CCDC90B
S. pombe_MCUR1
S. cerevisiae_YFL046W (Fmp32/Put6)
H. sapiens_MCUR1
H. sapiens_CCDC90B
MTS
TM
CCD
B
(NH4)2SO4
Proline
OD (600 nm)
Time (h)
Doubling time (h)
Sp-WT
Sp-MCUR1 KO
Sp-CCDC90B KO
Sp-Double KO
C
15N stable isotope enrichment
p value enrichment score
p value
[metabolite in Sp-Double KO]/[metabolite in WT]
L-pro-L-ile
L-pro
L-hpro-L-asp
L-pro-L-phe
L-hpro-L-gly
L-pro-L-pro
D
Lipid Set
Glycerophosphocholines
Glycerophosphoethanolamines
Fatty acyls
Fatty esters
Prenol lipids
Fatty acids and conjugates
Fatty alcohols
Glycerophospholipids
Glycerophosphoserines
Metabolite Set
Arginine and proline metab.
Arginine biosynth.
Alanine, aspartate and glutamate metab.
Purine metab.
Glutathione metab.
Glutamine and glutamate metab.
Aminoacyl-tRNA biosynth.
Nitrogen metab.
Glycine, serine and threonine metab.
Nicotinate and nicotinamide metab.
Glyoxylate and dicarboxylate metab.
beta-Alanine metab.
Histidine metab.
Pantothenate and CoA biosynth.
Valine, leucine and isoleucine biosynth.
Vitamin B6 metab.
Pyrimidine metab.
Cysteine and methionine metab.
Tryptophan metab.
Tyrosine metab.
Untargeted
Untargeted 15N stable isotope
p value
Enrichment ratio
E
L-asp
asn
L-ala
L-arg-suc
urea
L-pro-L-aa
L-ser
L-cys
gth
L-gly
L-arg
L-cit
4oxp
gcc
xan
hpro
L-pro
guan
L-orn
gua
gmp
p5c
put
N-ac-put
L-glu
4ab
spd
L-gln
4gdp
spm
xans
ino
imp
Arginine and proline metabolism
Alanine, aspartate and glutamate metabolism
Arginine biosynthesis
Polyamine biosynthesis
Glutathione metabolism
Purine biosynthesis
F
Sp-WT
Sp-MCUR1 KO
Hs-MCUR1 rescue
Sp-CCDC90B KO
Hs-CCDC90B rescue
Sp-Double KO
Hs-Double rescue

Figure 3

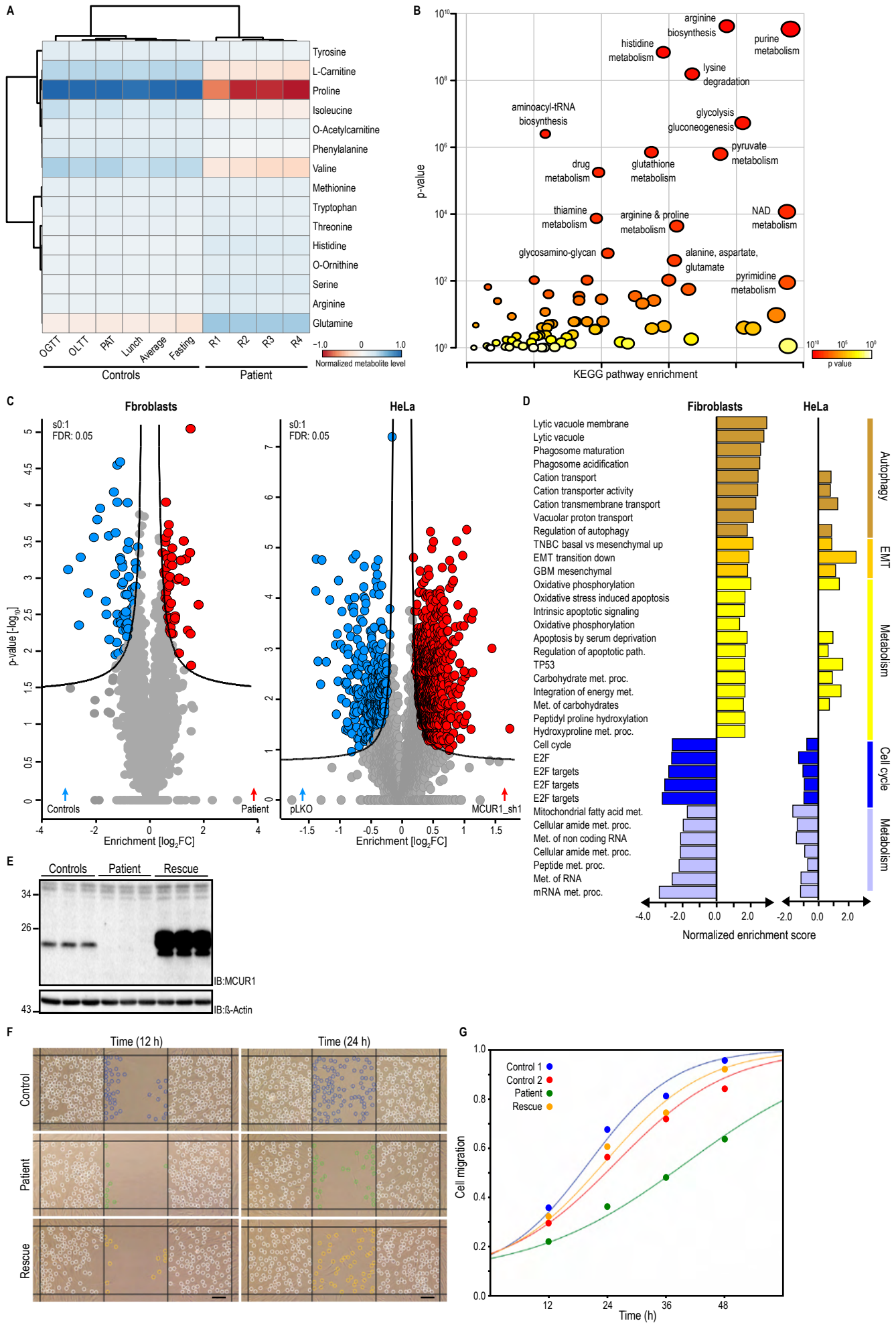
A
Tyrosine
L-Carnitine
Proline
Isoleucine
O-Acetylcarnitine
Phenylalanine
Valine
Methionine
Tryptophan
Threonine
Histidine
O-Ornithine
Serine
Arginine
Glutamine
OGTT
OLTT
PAT
Lunch
Average
Fasting
R1
R2
R3
R4
Controls
Patient
Normalized metabolite level
B
p-value
KEGG pathway enrichment
arginine biosynthesis
purine metabolism
histidine metabolism
lysine degradation
aminoacyl-tRNA biosynthesis
glycolysis gluconeogenesis
pyruvate metabolism
drug metabolism
glutathione metabolism
thiamine metabolism
arginine & proline metabolism
NAD metabolism
glycosamino-glycan
alanine, aspartate, glutamate
pyrimidine metabolism
p value
C
Fbroblasts
HeLa
s0:1
FDR: 0.05
p-value [-log10]
Enrichment [log2FC]
Controls
Patient
pLKO
MCUR1_sh1
D
Fibroblasts
HeLa
Lytic vacuole membrane
Lytic vacuole
Phagosome maturation
Phagosome acidification
Cation transport
Cation transporter activity
Cation transmembrane transport
Vacuolar proton transport
Regulation of autophagy
TNBC basal vs mesenchymal up
EMT transition down
GBM mesenchymal
Oxidative phosphorylation
Oxidative stress induced apoptosis
Intrinsic apoptotic signaling
Oxidative phosphorylation
Apoptosis by serum deprivation
Regulation of apoptotic path.
TP53
Carbohydrate met. proc.
Integration of energy met.
Met. of carbohydrates
Peptidyl proline hydroxylation
Hydroxyproline met. proc.
Cell cycle
E2F
E2F targets
E2F targets
E2F targets
Mitochondrial fatty acid met.
Cellular amide met. proc.
Met. of non coding RNA
Cellular amide met. proc.
Peptide met. proc.
Met. of RNA
mRNA met. proc.
Autophagy
EMT
Metabolism
Cell cycle
Metabolism
Normalized enrichment score
E
Controls
Patient
Rescue
IB:MCUR1
IB:ß-Actin
F
Time (12 h)
Time (24 h)
Control
Patient
Rescue
G
Control 1
Control 2
Patient
Rescue
Cell migration
Time (h)

Figure 4